Beneficial Effect of β-Cyclodextrin Assisted Synthesis of CuO/Hydroxyapatite Catalyst in Toluene Oxidation

Maya Ibrahim, Madona Labaki, Anne Ponchel, Jean-marc Giraudon, Olivier Gardoll, Jean-françois Lamonier

ChemCatChem

Research Article
doi.org/10.1002/cctc.202200943

Chemistry Europe
European Chemical Societies Publishing

www.chemcatchem.org

Beneficial Effect of β-Cyclodextrin Assisted Synthesis of CuO/Hydroxyapatite Catalyst in Toluene Oxidation

Maya Ibrahim,[a, b] Madona Labaki,[b] Anne Ponchel,[c] Jean-Marc Giraudon,*[a] Olivier Gardoll,[a] and Jean-François Lamonier[a]

Two hydroxyapatite supported CuO (10 wt% Cu) catalysts were prepared using the wet impregnation method *via* the conventional process and with the addition of native β-cyclodextrin using $Cu(NO_3)_2.3H_2O$ as copper precursor and adopting a ratio of β-cyclodextrin to copper of 0.1. After the impregnation step, the materials were dried at 80 °C and calcined in flowing dry air at 400 °C. The copper supported materials were characterized in the dried state and after calcination by means of conventional methods including X-ray diffraction, TG-MS, H_2-TPR-MS, Raman spectroscopy, UV-vis-DR, ToF-SIMS and XPS. It was found that β-cyclodextrin hasd a profound impact on the final properties of the catalysts, both in terms of reducibility and dispersion of active species. It is suggested that at the early stages of the calcination, some hydroxyl groups of the β-CD units in close contact with Ca^{2+} of hydroxyapatite could play the role of spacers between the copper-based entities thus minimizing the aggregation process of the CuO nanoparticles. Finally, these copper oxide catalysts prepared from β-cyclodextrin were able to oxidize toluene more efficiently than the conventional catalyst. The copper oxide particles generated by the thermal decomposition of $Cu_2(OH)_3(NO_3)$ were smaller than those formed with copper nitrate alone and exhibited a higher reducibility, two key determinants for VOC total oxidation on transition metal oxides.

Introduction

Toluene is regulated as a hazardous air pollutant and is subject to the emission limitations for various processes and operations in the synthetic organic chemicals manufacturing industry. Due to severe problems caused by toluene, different techniques for toluene abatement have been developed. Catalytic oxidation is one of the effective methods for toluene degradation as it oxidizes it to CO_2 and does not deliver other pollutants to the environment.[1–3] Catalysts can be divided into noble metal catalysts and transition metal oxide (TMO) catalysts.[4] Noble metals show excellent activities for the total oxidation of Volatile Organic Compound (VOC) at low temperatures[5,6] but have disadvantages such as being expensive, easy to sinter and easy to poison, which greatly limit their practical application. Compared to noble metals, TMO are cost-effective, superior resistance to poisoning and higher thermal stability.[7,8] Among the different TMO, CuO displays a good activity in toluene oxidation.[9,10] Notably, Al_2O_3 supported CuO_x show good performances in toluene oxidation.[11,12] Interestingly, it has been reported that a high density of weak acid sites is required for high toluene oxidation activity.[13]

Among the different types of support materials, hydroxyapatite ($Ca_{10}(PO_4)_6(OH)_2$, Hap, stoichiometric Ca/P = 1.67) which is the main component of bones and teeth has received increasing interest in recent years due to its remarkable properties including non-toxicity, stability (chemical, thermal), easy tailoring of the acid-base properties (through variation of the Ca/P ratio) and the ability to undergo cationic and anionic substitution. The combined properties of hydroxyapatites render them highly attractive for a wide range of applications.[14] and especially in heterogeneous catalysis.[15,16] Recently a new strategy in development of hydroxyapatite as promising noble-metal-free catalyst for VOC elimination and environmental cleaning techniques has emerged.[17] It is found that the predominant defect/oxygen vacancy generation in PO_4^{3-} site and enhanced basic site population established by selective mechanochemical activation of c-plane, facilitates the favorable catalytic oxidation route towards highly-efficient CO_2/CO conversion of VOC. The decomposition mechanism of VOC on stoichiometric HAp has been attributed to the generation of active oxygen radical during heating process. Such active radicals have been formed by the recombination of oxygen molecules and electrons trapped on Hap, which have been produced by the dehydration of –OH groups on c-plane of Hap.[18,19] This finding has prompt researchers to synthesize Hap structure with plenty of –OH groups such as ultralong Hap nanowires (NWs) which have attracted considerable attention due to their unique properties.[20] Indeed, Hap NWs alone[21] or as a heterojunction (Hap NWs@Co-MoF)[22] are able to activate

[a] M. Ibrahim, Dr. J.-M. Giraudon, O. Gardoll, Prof. J.-F. Lamonier
Univ. Lille, CNRS, Centrale Lille, Univ. Artois, UMR 8181
Unité de Catalyse et Chimie du Solide (UCCS)
Lille, 59000 (France)
E-mail: jean-marc.giraudon@univ-lille.fr
[b] M. Ibrahim, Prof. M. Labaki
Laboratory of Physical Chemistry of Materials (LCPM)/PR2 N
Lebanese University
Faculty of Sciences
Fanar, BP 90656
Jdeidet El Metn (Lebanon)
[c] Prof. A. Ponchel
Univ. Artois, CNRS, Centrale Lille, Univ. Lille, UMR 8181
Unité de Catalyse et Chimie du Solide (UCCS)
Lens, 62300 (France)

peroxomonosulfate (PMS) to degrade efficiently persistent water pollutants. Although the conversion of VOC leads to high global CO_x (x = 1, 2) yields, the conversion of VOC into CO_2 is rather low due to the lack of redox sites able to transform CO into CO_2. In a recent paper, Qu *et al.*[23] have explored the impact of different methods including ion exchange, co-precipitation and impregnation for the preparation of copper doped hydroxyapatite catalysts to adjust the location of Cu on hydroxyapatite and discussed the differences in catalytic performances for HCHO oxidation. Firstly, five possible locations for copper species supported on hydroxyapatite are proposed based on the features of hydroxyapatite and experimental results: (1) substitution of Ca^{2+} ions exposed on the surface Ca_S corresponding to dispersed Cu(II) clusters; (2) attached on the surface of hydroxyapatite (bulk CuO or $Cu_2(OH)PO_4$); (3) substitution of Ca_{II} (calcium ions at site II); site 4: substitution of Ca_I (calcium ions at site I) during the formation of $Ca_{19}Cu_2(PO_4)_{14}$); (5) in the c-axis oriented channel (CuO particles). It is found that the method of preparation has a profound impact on the location of Cu species. While both impregnation and co-precipitation resulted in high content of surface Cu species in the form of bulk CuO along with some channel CuO particles (impregnation) and Cu species occupying Ca_I sites (co-precipitation), ion-exchange favor the substitution of Ca_S sites leading to dispersed Cu(II) clusters found to be the most active in oxidation of formaldehyde. However, ion-exchange resulted in a three-fold decrease of the Cu content in the hydroxyapatite, contrarily to the other two methods.

Our group has previously investigated the effect of copper loading on hydroxyapatite using wet impregnation.[24] Better activity and good stability over time in toluene oxidation observed for the lowest Cu loading (2.5 wt%) is ascribed mainly to well dispersed CuO nanoparticles on hydroxyapatite and possibly because of the participation of hydroxyapatite in toluene activation. Notably, an increase in metal loading results in copper oxide particle agglomeration and therefore in a decrease of catalytic activity. These results prompt us to select another strategy of catalyst preparation to improve Cu dispersion and redox properties based on the addition of β-cyclodextrin (β-CD) during the wet impregnation step.

β-CD is a cyclic oligosaccharide consisting of seven α-(1-4)-linked D-glucopyranose units. It is a hollow cone-shaped molecule with an exterior hydrophilic surface and interior electron-rich hydrophobic cavity of 0.79 nm depth, which is capable of forming stable, supramolecular structures.

Cyclodextrins (CDs) take advantage of their hydrophobic cavity and their two hydrophilic rims to form host-guest complexes[25] and supramolecular adducts,[26–28] respectively. As a consequence, cyclodextrins and their derivatives have found applications in many areas, for example in drug carrier systems, food industry, cosmetics, remediation and catalysis.[29]

Regarding heterogeneous catalysis the first application of cyclodextrins in the preparation of supported heterogeneous catalysts using aqueous impregnation has been reported for the design of alumina supported catalyst efficient in Fischer-Tropsch synthesis.[30] The structure and catalytic performance of alumina supported cobalt catalysts for Fischer–Tropsch synthesis are profoundly affected by the addition of β-CD during catalyst preparation. Impregnation of alumina with solutions containing β-CD leads to higher metal dispersion and exceedingly enhances both reaction rate and heavy hydrocarbons productivity. The use of β-cyclodextrin during the impregnation step seems to increase the crystal nucleation site density which can be associated to the complexes of cobalt with β-cyclodextrin or to the products of its decomposition. The observed activity, almost four times higher than without the use of β-CD has been mainly ascribed to the enhancement of cobalt dispersion.

Later, the pivotal role of β-cyclodextrin, among others, has been particurlarly investigated in assisted synthesis of supported TMO catalysts for VOC oxidation. L. Bai *et al.*[31] have reported the effect of β-cyclodextrin on the genesis of zirconia supported cobalt oxide phase to be related on their performances in the total oxidation of formaldehyde. It turns out that β-CD has a strong impact on the final structure of the catalysts, in terms of reducibility and dispersion of active species. The starting interactions between β-CD and $Co(NO_3)_2$ in solution and in the dried solid states after impregnation on the support are known to be of fundamental importance to control the nucleation and growing processes of metal oxide species. The authors postulate the formation of supramolecular adducts between β-CD and Co^{2+} and NO_3^- The catalytic results indicate that the better-dispersed $CoCD_{0.1}$/Zr (Co/CD molar of 0.1) catalyst with enhanced reducibility of cobalt exhibits the highest conversion of formaldehyde into CO_2. Regarding the role of β-CD in Co dispersion and catalytic performance, it can be invoked that supramolecular adducts are formed between β-CD and Co^{2+} as well as NO_3^-. Knowing that the native β-CD is a polyhydroxylated molecule containing 21 hydroxyl groups, the optimal effect obtained at the ratio of 0.1 (in other words, 2.1 OH groups per cobalt atom) can be rationalized by invoking the formation of supramolecular adduct of Co^{2+} with β-CD, in which the cobalt center would interact with two O atoms from the outside rims of the β-CD. Cyclodextrin can be considered as scaffold molecule that concentrates the cobalt ions at its close vicinity and leads to the formation of more stable complexes of cobalt ions with β-CD and its oxidation products formed during calcination. These complexes minimize the aggregation process by preventing the interactions of cobalt ions together and their subsequent decomposition results in the formation of smaller and more reducible cobalt oxide particles on zirconia.

In a subsequent paper,[32] the same team has reported on the use of β-CD during the preparation of zirconia-supported cobalt oxide catalysts by impregnation with respect to three cobalt precursors (i.e. cobalt nitrate, acetate and acetylacetonate). The effect of β-CD is carefully discussed at different stages of the material preparation. It is found again that β-CD has a strong impact on the final properties of the catalysts, both in terms of reducibility and dispersion of active species. The results are rationalized to the occurrence of complexation between the cobalt precursor and β-CD and highlight the pivotal role played by the counter-anion. The best combination is obtained using cobalt nitrate with a β-CD/cobalt ratio 0.1 and the beneficial impact of cyclodextrin for the impregnation

method have been successfully extended to other cyclodextrins such as α-CD and γ-CD.

Recently, the facile CD-assisted co-impregnation method has been used to prepare a highly active CuO-CeO_2 catalyst dispersed on mesoporous silica foam (MCF) after calcination at 450 °C for CO oxidation.[33] Compared with a reference catalyst synthesized by a conventional method, the one prepared by CD-assisted method has higher activity and stability in CO oxidation. A higher dispersion, an enhanced homogeneous distribution of the active components (Cu and Ce), more Ce^{3+} and Cu^{+} species linked to surface defects have been invoked as contributing to the higher catalytic performances in CO oxidation.

Based on these previous results, the objective of the present work is to apply the concept of β-cyclodextrin assisted synthesis for the design of hydroxyapatite supported copper oxide catalyst containing 10 wt% copper with improved catalytic properties in toluene total oxidation. On purpose, two catalysts have been prepared by wet impregnation starting from copper nitrate as copper precursor without and with β-cyclodextrin added in a non-stoichiometric amount (β-CD/Cu = 0.1). The samples have been then dried at 80 °C and calcined at 400 °C. Characterizations for dried and calcined samples with β-CD additive and catalytic results have been systematically compared with the data obtained for the reference copper catalyst prepared without β-cyclodextrin.

Results and Discussion

Dried precursors

Structural characterization

X-Ray Diffraction (XRD)

The powder X-ray diffraction patterns of the dried 10 Cu/Hap D and 10 Cu-CD/Hap D samples are shown in Figure 1-a. The XRD diffractograms of both compounds display the characteristic peaks relative to the hexagonal hydroxyapatite phase (PDF 00-009-0432) with a P63/m space group. Additional peaks located at 2θ = 12.8° and 36.5° in both 10 Cu/Hap D and 10 Cu-CD/Hap D diffractograms are ascribed to copper hydroxynitrate with $Cu_2(OH)_3(NO_3)$ formula, naturally found in the mineral called gerhardtite (PDF 75-1779).

This basic Cu(II) salt, which is known to be formed by careful heating of $Cu(NO_3)_2.3H_2O$ at 80 °C,[34–35] has been previously shown on dried copper-loaded hydroxyapatite systems using incipient wetness impregnation method.[36]

The mean crystallite size of copper hydroxynitrate, based on the Scherrer equation from the peak located at 2θ = 12.8°, is of the same order of magnitude for the 10 Cu/Hap D and 10 Cu-CD/Hap D samples with values of 84 nm and 96 nm, respectively. The presence of multiple peaks in the 10–25° 2θ range characteristic of the XRD pattern of pure β-CD (Figure 1-b) in accordance with literature reports[37–38] are not observed for 10 Cu-CD/Hap D sample, suggesting a homogeneous distribution of β-CD in the material.

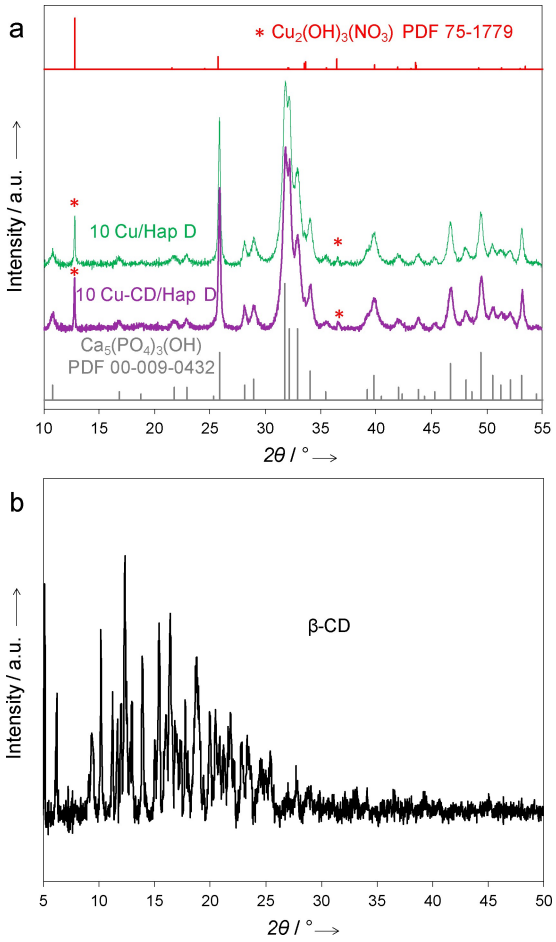

Figure 1. XRD patterns of a) 10 Cu/Hap D, 10 Cu-CD/Hap D and of b) pure β-CD.

ToF-SIMS

The interactions between copper and hydroxyapatite with β-cyclodextrin or its degradation products have been investigated using ToF-SIMS. Figure 2 shows the superposition of the ToF-SIMS spectra for the dried samples in polarity (+) in the 90.60-94.60 m/z range. It is possible to observe intense secondary ions at m/z 90.9217, 91.9295, 92.9264 which can be ascribed to $CuOC^{+}$, $CuHOC^{+}$ and $^{65}CuOC^{+}$ for 10 Cu-CD/Hap D. The presence of these ions strongly supports the favorable interaction of the cyclodextrin degradation by-products with Cu. Additionally it can be observed secondary ion at m/z 68.961 being ascribed to $CaOCH^{+}$ which shows that β-cyclodextrin degradation by-products interact with the Lewis acid sites Ca^{2+} of the hydroxoapatite. This finding agrees with previous study highlighting that the hydroxyl groups of β-CD are the major interaction sites between Ca^{2+} and β-CD.[39]

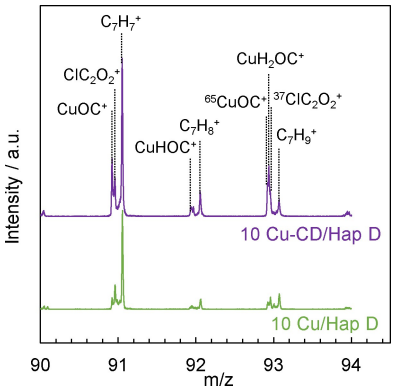

Figure 2. ToF-SIMS spectra of 10 Cu/HapD and 10 Cu-CD/HapD in polarity(+) in the 90.60-94.60 m/z range.

Raman spectroscopy

The Raman spectra of different grains (A–F) of 10 Cu/Hap D are shown in Figure 3-a. Differences appear between the various spectra, both in terms of lines positions and intensity, highlighting a great heterogeneity of the solid. It is always observed the characteristic modes of vibration of PO_4^{3-} of the Hap support located at 961 cm^{-1} (ν_1 symmetric stretching of P–O), 428 and 445 cm^{-1} (ν_2 bending modes of O–P-O), 578, 590, and 606 cm^{-1} (ν_4 mode).[40] The Raman spectrum A shows Raman lines at 256, 278, 332, 407, 500, 709, 718, 745, 1047, 1320, and 1439 cm^{-1} which can be ascribed to the characteristic lines of $Cu_2(OH)_3(NO_3)$.[41,42] Most interestingly, the Raman spectra C–F exhibit two modes of vibration at about 290 and 646 cm^{-1} which can be ascribed to the A_g and B_{2g} modes of CuO, respectively,[43] indicating the formation of some CuO particles during the drying step. By opposition, the Raman spectra of different grains (A–F) of 10 Cu-CD/Hap D shown in Figure 3-b are rather similar showing a good homogeneity of the sample. It is only observed, alongside the different vibration modes of PO_4^{3-}, the vibration modes of $Cu_2(OH)_3(NO_3)$ without the presence of CuO. This last finding agrees with the work of Bai *et al.*[31] who reported absence of transition metal oxide in the presence of β-CD during the drying step.

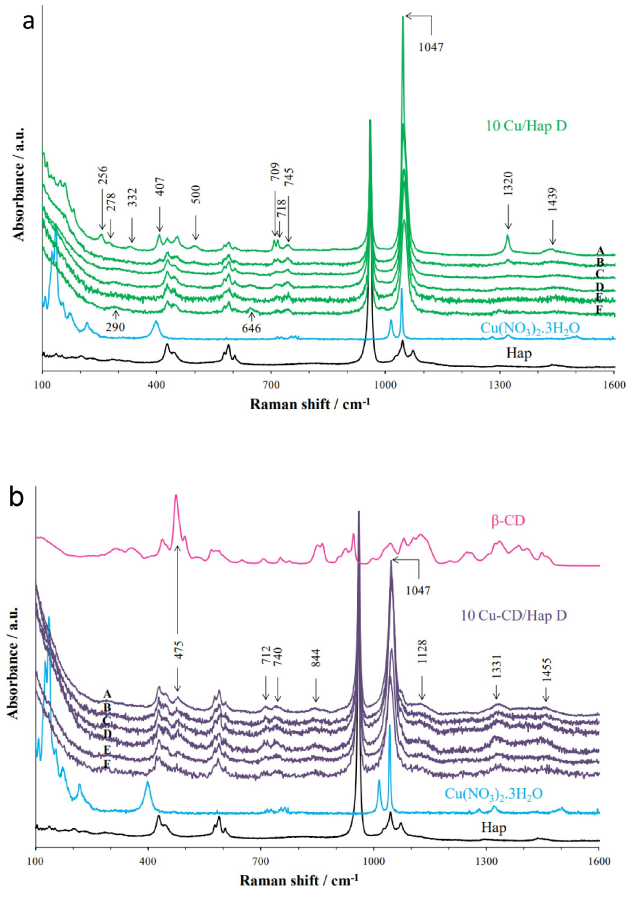

Figure 3. Raman spectra of a) Hap, $Cu(NO_3)_2.3H_2O$, and 10 Cu/Hap D, b) Hap, $Cu(NO_3)_2.3H_2O$, β-CD, and 10 Cu-CD/Hap D materials (A, B, C, D, E and F correspond to spectra obtained for different grains of sample).

Decomposition of the dried impregnated 10 Cu/Hap D and 10 Cu-CD/Hap D samples

Thermal analysis coupled with mass spectrometry (TGA-DSC/MS)

A thermogravimetric analysis coupled with mass spectroscopy was carried out in order to investigate the effect of β-CD on the degradation pathway of the supported Cu precursors in dry air on the dried solids, after impregnation on hydroxyapatite, solvent evaporation and drying at 100 °C. Figures 4-a and 4-b show the TGA/DTG and TGA/DSC traces of the solid transformation and the temperature programmed desorption profiles of H_2O (m/z 18), CO_2 (m/z 44), NO (m/z 30) and NO_2 (m/z 46) detected in the course of the solid transformation carried out on 10 Cu-CD/Hap D and 10 Cu/Hap D. The weight losses inherent to these transformations are displayed in Table 1.

Without β-cyclodextrin, a total weight loss of 17.6 wt% is observed within the whole temperature range from 20 °C to 600 °C. The DTG curve shows three peaks at 65 °C, 320 °C and 415 °C corresponding to three distinct steps. The first endothermic step is associated with the release of adsorbed water[44] in line with H_2O evolution (m/z = 18, 17; Figure 4-c). The second weight loss which takes place between 200 °C and 400 °C associated with concomitant NO (Figure 4-d) and H_2O (Figure 4-c) release can be the result of the slow and continuous thermal decomposition of the copper hydroxynitrate[34–35] generating CuO *via* H_2O and HNO_3 removal which decomposes rapidly into

Table 1. TGA based data for 10 Cu/Hap D and 10 Cu-CD/Hap D solids.

Sample	Global weight loss [%]	Experimental weight loss [%]		
		1st step	2nd step	3rd step
10 Cu/Hap D	17.6	4.1 (20–200 °C)	11 (200–400 °C)	1.2 (400–450 °C)
10 Cu-CD/Hap D	26.6	3.1 (20–120 °C)	6.4 (120–190 °C)	15.1 (190–350 °C)

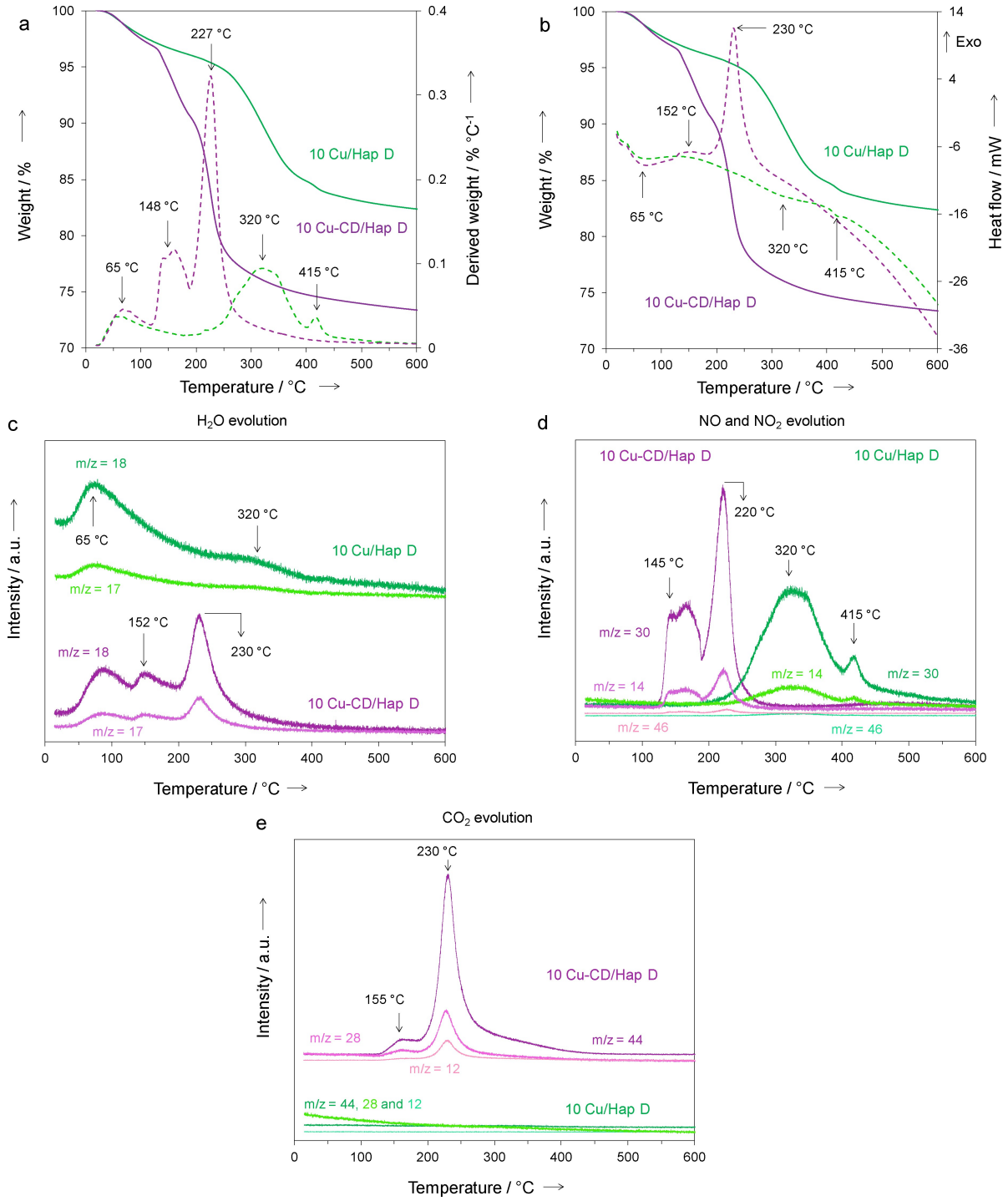

Figure 4. TGA-DTG a), TGA-DSC b) and MS signals corresponding to the evolution of H_2O (c), NO, NO_2 (d), and CO_2 (e) in 10 Cu/Hap D and 10 Cu-CD/Hap D sample.

NO and NO_2.[45–46] Finally, the third endothermic step, characterized by a weight loss of around 1.2 wt%, occurring between 400 °C and 450 °C can be due to the decomposition of remaining nitrate species probably incorporated in the Hap support in line with NO removal.

The introduction of β-CD as additive at a ratio of 0.1 has a significant effect on the thermal decomposition of the copper entities adsorbed on hydroxyapatite surface. Indeed, the TG curve is shifted to lower temperature indicating easier degradation of the Cu entities. As expected, a higher total weight loss of 26.6 wt% is observed due to the presence of β-CD. The DTG trace reveals again a three-step decomposition process with peak temperatures located at 65 °C, 148 °C and 227 °C (Figure 4-a). The first endothermic process leading to a slight weight loss

of 3.1 wt%, observed from 20 °C to 120 °C, is due to the release of adsorbed water as well consistent with the evolution of signal intensity for m/z = 17 and 18 (Figure 4-c). By opposition the second and third exothermic processes taking place at 120 °C–190 °C and 190 °C–350 °C are accompanied by the release of H_2O, CO_2 (Figure 4-e) and NO/NO_2.

Based on the trace of m/z = 30, it is found that the nitrate thermal decomposition starts at 120 °C as compared to 200 °C for 10 Cu/Hap D. These nitrate species are supposed to belong to the gerhardtite in close vicinity of β-CD in accordance with simultaneous release of H_2O and CO_2, although the release of H_2O can also arise from water molecules present in the cavity of the β-CD.[47] The third process is consistent with the complete degradation of $Cu_2(OH)_3(NO_3)$ to generate NO/NO_2 and H_2O and of the concomitant degradation and oxidation of β-CD to give CO_2 and H_2O. Thus, while it is observed that β-CD starts to decompose at about 150 °C, the major weight loss occurs at 227 °C. Note that these temperatures are significantly lower than the temperatures observed for the thermal degradation of β-CD (300–320 °C) when impregnated on hydroxyapatite support,[48] in rather similar conditions, but in the absence of copper salt. TG profiles with similar temperature ranges ~ 300 °C have been also obtained for β-CD in the bulk state.[49] Knowing the oxidizing potential of copper and nitrate species, this shift toward lower temperatures may again be indicative of the proximity of β-CD to the copper and nitrate ions on hydroxyapatite surface. Finally, the constant weight loss observed after 450 °C (1.3 wt%, 10 Cu/Hap D) and 350 °C (2 wt %, 10 Cu-CD/Hap D) is mainly due to the dehydroxylation of the Hap.[50–51]

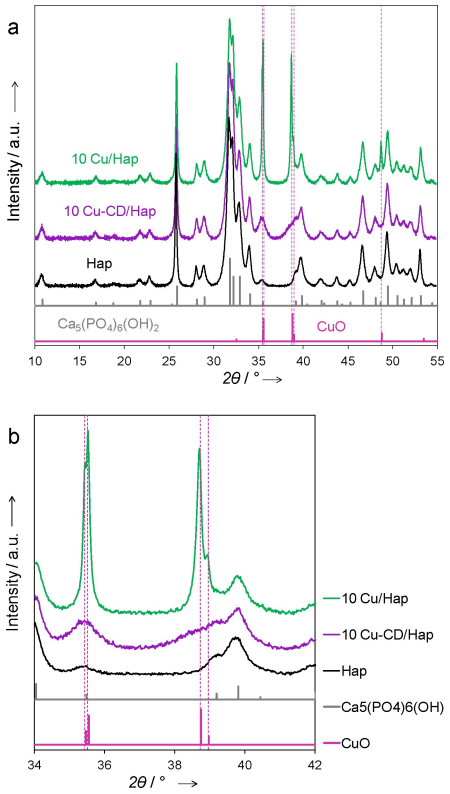

Figure 5. a) XRD patterns of 10 Cu/Hap, 10 Cu-CD/Hap and Hap samples; b) a zoom in the 2θ range of 34–42°.

Calcined catalysts

Structural characterization

X-Ray Diffraction (XRD)

To get more information on the effect of the β-CD addition on the structural characteristics of the copper-supported hydroxyapatite solids after calcination, the two calcined samples have been further analyzed by wide angle X-ray diffraction. The corresponding X-ray diffractograms are shown in Figure 5-a with a zoom in the 2θ range of 34–42° (Figure 5-b) showing the dominant CuO (111) and (11-1) diffraction peaks with a monoclinic structure (tenorite, PDF n° 00-048-1548). We observe that, after the impregnation of the copper precursor and the subsequent calcination, there is no modification of the crystallographic features of the hydroxyapatite support in the hexagonal phase (PDF n° 00-009-0432) in terms of intensity and peak position. These results indicate that the addition of copper does not interfere with the structure of hydroxyapatite to some extent. The two intense reflection peaks at 2θ = 35.5° and 38.8° as well as a less intense peak at 2θ = 48.7° show that CuO nanocristallites can be formed upon calcination in air at 400 °C. The average crystallite size estimated from the FWHM of the peak at 2θ = 48.7° to get rid of peak overlapping occurring for the most two intense peaks (Figure 5-b) using Scherrer equation is 45 nm in accordance with previous results.[22] Notably, a significant reduction in the intensity and broadening of the peaks relative to CuO are observed for the calcined β-CD sample indicating that the average crystallite size of copper oxide strongly decreases to a value of 14 nm. This indicates that the presence of the β-CD or its degradation products at the early stages of the calcination in close interaction with the copper entities prevents the growth of large particles of CuO.

Raman spectroscopy

Optical visualization of the 10 Cu/Hap and 10 Cu-CD/Hap samples reveals bright and dark zones. The bright-contrast and the dark-contrast zones are defined as hydroxyapatite and copper oxide enriched zones, respectively. Figures 6-a and 6-b present typical Raman spectra of grains belonging to the bright and dark zones of 10 Cu/Hap and 10 Cu-CD/Hap to be compared with that of pure Hap. The Raman spectra of the bright areas of both samples are rather similar to that of pure Hap showing the four active ν_1, ν_2, ν_3 and ν_4 vibrational modes of PO_4^{3-}, the only differences being those in the width and relative intensity of the lines. In particular, it is noticed that the full width at half maximum (FWHM) of the most intense ν_1 vibrational mode increases owing to: 6.9 (Hap) < 7.5 (10 Cu-CD/Hap) < 8.9 cm^{-1} (10 Cu/Hap) indicating a decrease in the crystallinity of Hap. The typical spectra of the dark zone for both samples shows the three Raman active modes Ag and 2Bg

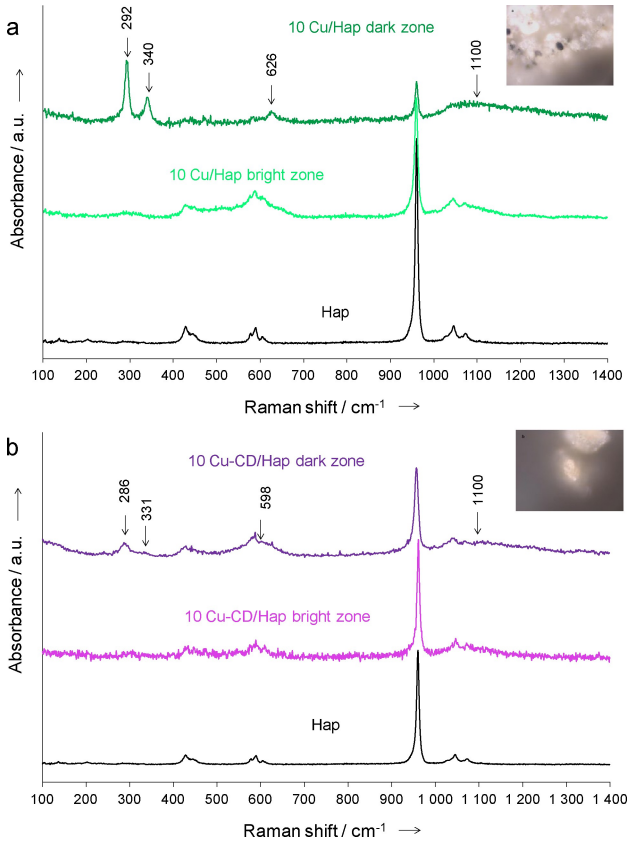

Figure 6. Raman spectra of a) Hap, 10 Cu/Hap bright zone, 10 Cu/Hap dark zone b) Hap, 10 Cu-CD/Hap bright zone, 10 Cu-CD/Hap dark zone.

relative to the monoclinic structure of CuO which is described by the C_{2h} space group. The Raman spectrum of 10 Cu/Hap displays three distinct lines at 292 cm^{-1}, 340 cm^{-1} and 626 cm^{-1} which correspond to the Ag, Bg (1) and Bg (2) modes of the CuO single crystal, respectively.[52] By opposition, it is now observed large peaks of low intensity located downshift at 286 cm^{-1}, 331 cm^{-1} and 598 cm^{-1} for 10 Cu-CD/Hap related to small CuO NP. The broadenings and red shifts of the Raman lines can be mainly attributed to the quantum confinement effect of the CuO nanoparticles[53] in line with size effects[52] which agree with XRD results.

Besides, it is observed for 10 Cu-CD/Hap (dark zone) that the position of the main line of Hap (ν_1 mode of PO_4^{3-}) is red-shifted from 961.0 cm^{-1} (Hap) to 956 .1 cm^{-1} and that the line clearly broadens as the measured FWHM increases from 7.2 cm^{-1} (Hap) to 10.4 cm^{-1}. This line broadening and red shift can be associated to the decrease of crystallinity of the sample linked to the change in the PO_4^{3-} surrounding implying an increase of the P–O bond distances. This finding can be related to the incorporation of some Cu^{2+} in the Hap structure as previously observed in the literature.[54]

Speciation of copper (II)

UV-visible/DR

The UV-vis diffuse reflectance spectra of the dried and calcined samples at 400 °C are shown in Figure 7. As pure hydroxyapatite Hap shows only a band at 205 nm ascribed to O^{2-}-Ca^{2+} charge transfer,[55] the new bands for Cu based samples can be ascribed to copper related species. Both dried samples show similar spectra consisting of an intense absorbance band in the UV range centered at about 260 nm which can be ascribed to O^{2-}-Cu^{2+} charge transfer transitions[56] and a very large band starting from 540 nm to extend beyond 900 nm which can be due to d-d transitions of Cu^{2+} in accordance with the two different distorted octahedral sites within the layer of copper hydroxynitrate $Cu_2(OH)_3NO_3$.[57]

The blue color of the uncalcined samples transform into gray and brown after the calcination step for Cu10/Hap and 10 Cu-CD/Hap, respectively. The spectrum of 10 Cu/Hap sample shows a large band in the 600–900 nm range with a maximum at 750 cm^{-1} which can be assigned to d-d transitions of Cu^{2+} in a tetragonal distorted octahedral Oh configuration indicative of the formation of dispersed CuO particles,[58] in agreement with XRD results. Additionally, the absorption bands in the 290–400 nm range can be assigned to Cu^{2+}-O^{2-}-Cu^{2+} charge transfer.[59] The calcination step of the 10 Cu-CD/Hap D sample provokes the appearance of CuOx three-dimensional clusters highlighted by the presence of absorption bands region at 325 nm and 440 nm assigned to Cu^{2+}-O^{2-}-Cu^{2+} charge transfer.[60] A band at about 715 cm^{-1} can be assigned again to d-d transitions of Cu^{2+} in a tetragonal distorted octahedral Oh configuration.

Redox characterization

Temperature programmed reduction coupled with mass spectrometry (H_2-TPR-MS)

The reducibility of copper oxide to metallic copper is assessed by H_2-temperature programmed reaction - mass spectrometry. The

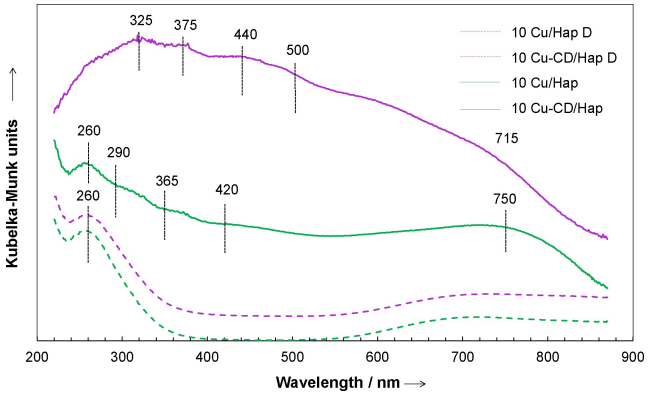

Figure 7. UV-vis diffuse reflectance spectra of the dried and calcined samples at 400 °C.

H_2-TPR profiles of the copper catalysts are given in Figure 8 and the temperature programmed desorption profiles of H_2O (m/z 18), CO_2 (m/z 44), NO (m/z 30) and NO_2 (m/z 46) are exhibited in Figure 9 while Table 2 lists the results in terms of H_2 consumption and starting temperature of reduction. In both cases, the total hydrogen consumed in the whole H_2-TPR experiment exceeds the theoretical amounts required for the complete reduction of copper ions in the CuO phase, from the oxidation state +II to 0. Taken these results into account, it is suggested the participation of remaining reducible species such as NO_3^-/CO_3^{2-} incorporated in the hydroxyapatite lattice to report on this hydrogen over-consumption which is higher without β-CD additive. The H_2-TPR profile of the sample prepared without β-CD exhibits three distinct H_2 consumption peaks. The first H_2-TPR peak at 234 °C is attributed to the reduction of remaining nitrate species in line with the release of NO (m/z = 30) while the second more intense peak (250 °C–375 °C) corresponds to the reduction of CuO into metallic Cu. The high-temperature peak with a peak maximum at 450 °C is ascribed to the reduction of nitrate species trapped in hydroxyapatite into N_2 (m/z = 28, m/z = 14) and NH_3 (m/z = 17, m/z = 16). Such evolution of gaseous nitrogen species as a function of temperature follows the reaction scheme of the catalytic hydrogenation of nitrate species over copper bearing materials proposed in previous investigations[61–62] and represented by scheme 1:

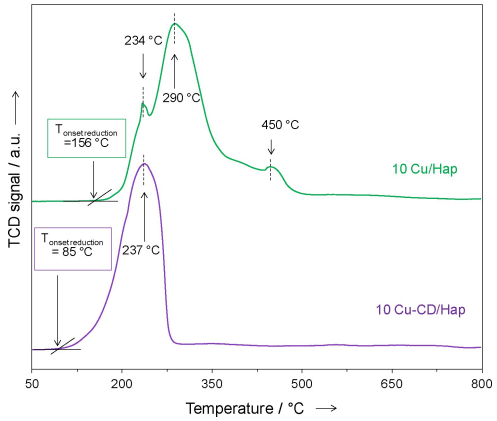

Figure 8. H_2-TPR profiles of 10 Cu/Hap and 10 Cu-CD/Hap solids calcined at 400 °C.

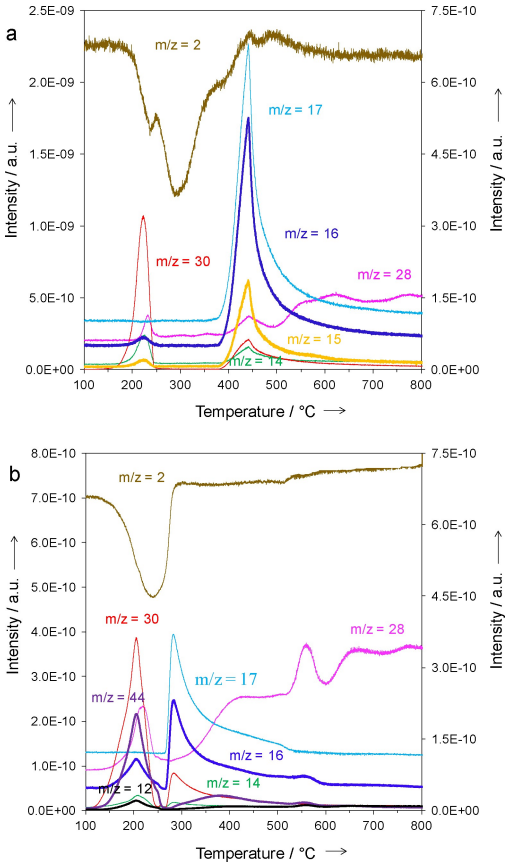

Figure 9. Evolution of the intensity of the signals corresponding to m/z = 2 (given by the y-axis on the right), 12, 14, 15, 16, 17, 28, 30, and 44 (given by the y-axis on the left) as a function of temperature for the solids: a) 10 Cu/Hap and b) 10 Cu-CD/Hap.

Table 2. H_2-TPR results.

Sample	$T_{onset\ reduction}$ [°C] [a]	T_{NO} [°C] [b]	$n(H_2)_{th}$ [c] [mmol.g^{-1}]	$n(H_2)_{exp}$ [d] [mmol.g^{-1}]
10 Cu/Hap	156	150	1.58	2.81
10 Cu-CD/Hap	85	110	1.58	1.99

[a] Temperature of onset reduction. [b] Temperature of NO appearance. [c] Theoretical amount of H_2 consumed. [d] Experimental amount of H_2 consumed.

To overcome the problem of reduction of nitrate species at low temperature, the reducibility of the solids is determined from the temperature corresponding to the onset of NO production (T_{NO}) knowing the capacity of Cu(0) to reduce NO_3^- species into NO at low temperature. The most reducible solid is thus the one with the lowest value of T_{NO} (°C): 10 Cu-CD/Hap (110) < 10 Cu/Hap (150). Such a beneficial effect of β-CD on the reducibility, already observed in the literature,[31–32] can be related to the intimate contact between β-CD and copper species taking place during the

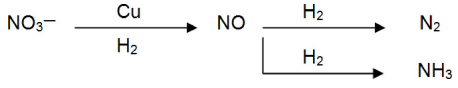

Scheme 1. Reaction scheme of the catalytic hydrogenation of nitrate on Cu-based catalysts.

first stages of the calcination. β-CD or its decomposition products can act as spacers which prevent the sintering of the CuO particles produced from the decomposition of $Cu_2(OH)_3(NO_3)$, then resulting in a decrease of the nano copper oxides particles weakly interacting with the hydroxyapatite support.

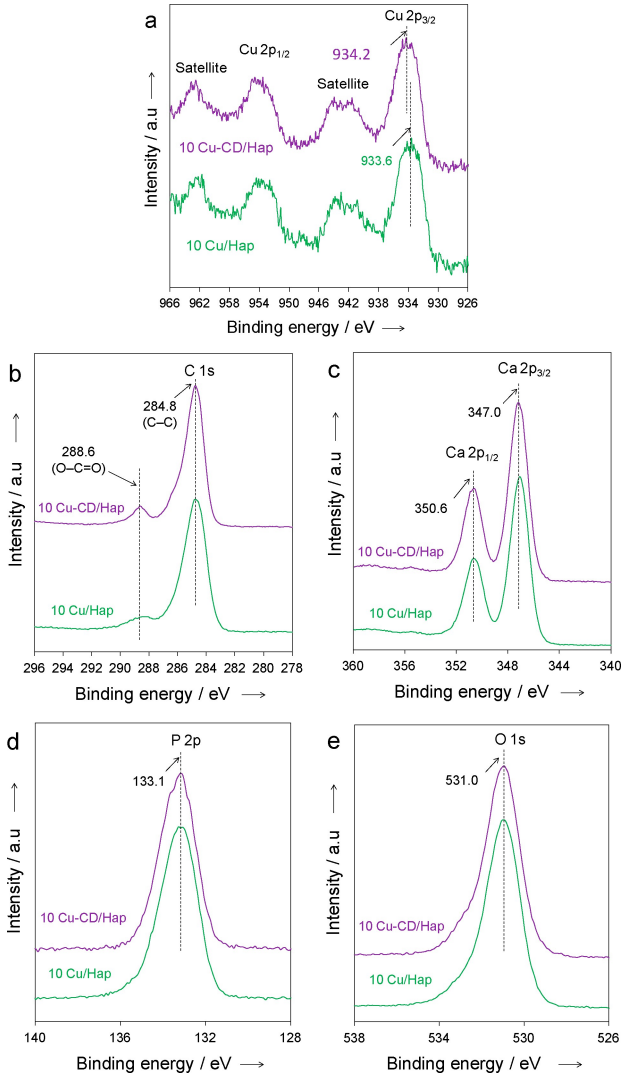

Figure 10. (a) Cu 2p, (b) C1s, (c) Ca2$p_{3/2}$, (d) P2p and (e) O1s XPS core levels for 10 Cu/Hap and 10 Cu-CD/Hap materials.

Surface characterizations

X-ray photoelectron spectroscopy (XPS)

XPS characterization of the calcined samples has been investigated in order to get insight into the valence state of copper and its relative dispersion on the hydroxyapatite support. The Cu 2p core level XPS spectra are given in Figure 10-a and the quantitative data are gathered in Table 3. For the calcined copper sample without addition of β-CD, the BE of Cu $2p_{3/2}$ at 933.6 eV and the satellite to the main Cu $2p_{3/2}$ peak (I_{sat}/I_{pp}) intensity ratios of 0.50 compare well to the values of 933.6 eV and 0.53 found for a bulk copper oxide.[63] For the sample with β-CD additive, the Cu $2p_{3/2}$ peak position is now observed at a higher BE of 934.2 eV and the I_{sat}/I_{pp} value is 0.55. These results are consistent with the presence of copper oxide particles dispersed on hydroxyapatite which interact more strongly with apatite in the presence of cyclodextrin additive. Notably, the ratio of copper to the sum of calcium and phosphorus surface concentrations Cu/(Ca + P) measured by XPS of 0.06 doubles when using β-CD. The copper enrichment at the surface of hydroxyapatite for 10 Cu-CD/Hap once again suggests supported copper oxide particles of smaller sizes.[64] For both 10 Cu/Hap and 10 Cu-CD/Hap, Ca $2p_{3/2}$, P 2p and O1s photopeaks (Figures 10-c, 10-d and 10-e) were found to be, respectively, located at 347.0, 133.1 and 531,0 eV, values which are typical of hydroxyapatite material.[65]

Regarding the presence of any residual carbonaceous based entities in 10 Cu-CD/Hap, no additional feature or significant increase in the intensity of the peaks noted in C1s core level spectrum can be seen for 10 Cu-CD/Hap when compared to 10 Cu/Hap sample (Figure 10-b). The evaluation of the relative proportions of phosphate and calcium ions exposed at the surface of Hap was performed through the determination of the Ca/P ratios from the peak corresponding to the Ca 2p and P 2p core levels. It is worthy to note that the Ca/P ratio of 10 Cu/Hap of 1.50 is similar to that of the Hap calcined at 400 °C of 1.49. However, the Ca/P ratio of 1.35 for 10 Cu-CD/Hap is lower than that of the 10 Cu/Hap which might indicate that the presence of β-cyclodextrin could have an effect on the Ca^{2+}/PO_4^{3-} surface distribution. However, the surface terminations of crystalline hydroxyapatite particles which can be enriched either in calcium or in phosphate species, play a crucial role in reactivity and raises the question of whether the XPS method is reliable in characterization the top layer of the sample. For this purpose, it has been previously shown that LEIS which is a sensitive technique to probe the top layer of the different Haps indicates an enrichment of Ca while XPS data conclude to lower Ca/P ratios.[66]

Table 3. XPS based data for 10 Cu/Hap and 10 Cu-CD/Hap.

Sample	Cu $2p_{3/2}$ BE	FWHM[a] Cu $2p_{3/2}$	Cu $2p_{1/2}$ BE	FWHM[a] Cu $2p_{1/2}$	I_{sat}/I_{pp} [b]	Ca/P[d]	Cu/(Ca + P)[d]
10 Cu/Hap	933.6	3.9	953.7	4.4	0.50 [0.47][c]	1.50	0.06
10 Cu-CD/Hap	934.2	3.8	954.5	4.4	0.55 [0.53][c]	1.35	0.13

[a] Full width at half maximum. [b] Intensity ratio between Cu $2p_{3/2}$ and corresponding satellite peak. [c] Intensity ratio between Cu $2p_{1/2}$ and corresponding satellite peak. [d] XPS atomic ratio.

Catalytic performances in the total oxidation of toluene

Toluene oxidation light-off curves (toluene conversion-temperature plot) for 10 Cu/Hap and 10 Cu-CD/Hap are shown in Figure 11. The comparison of the two curves clearly shows the beneficial effect of the addition of cyclodextrin during the preparation of the catalyst. Cu-CD/Hap outperforms Cu/Hap whatever the reaction temperature and a T_{50} (toluene) of 232 °C and 253 °C is respectively obtained. The catalytic performances of 10 Cu/Hap and 10 Cu-CD/Hap and some platinum-supported (Al_2O_3, SiO_2 and TiO_2) catalysts tested in the total oxidation of toluene are reported in Table 4. Our best performing catalyst, *i.e.* 10 Cu-CD/Hap, shows comparable activity to Pt-supported catalysts. The catalytic properties of the various Cu-based materials obtained in the total oxidation of toluene have already been recently overviewed by our group.[24] Compared to copper-based catalysts supported on classical supports such as alumina, titania and silica,[24] 10 Cu-CD/Hap is significantly more active in toluene total oxidation. The comparisons above clearly highlight the key contribution of the cyclodextrin towards the development of low cost and high-performance catalytic systems for toluene total oxidation.

The catalytic performances of the copper oxide catalysts have been finally assessed in the complete oxidation of toluene for different inlet concentrations as a function of time. Figures 12-a and 12-b show the toluene conversion as a function of time (24 h) at 250 °C for three successive different inlet toluene concentrations

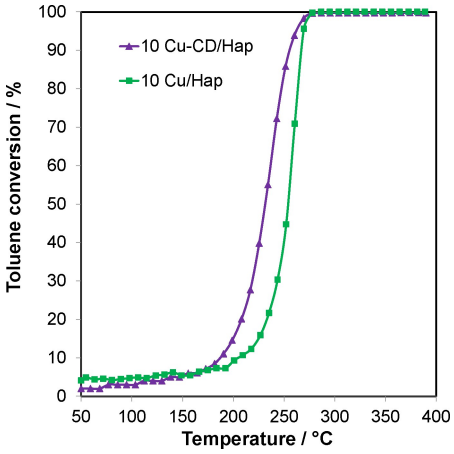

Figure 11. Light-off curves for the toluene oxidation in the presence of 10 Cu/Hap and 10 Cu-CD/Hap catalysts.

Table 4. Toluene concentration, VHSV, T_{50} on our catalysts and conventional Pt based catalysts.

Catalyst	Toluene [ppm]	VHSV [$L.g^{-1}.h^{-1}$]	T_{50} toluene [°C]	Reference
10 % Cu-CD/Hap	800	30	232	Present work
10 % Cu/Hap	800	30	253	Present work
0.5 % Pt/Al_2O_3	1000	200	205	[67]
0.5 % Pt/SiO_2	1000	200	205	[67]
0.5 % Pt/TiO_2	1000	200	230	[67]

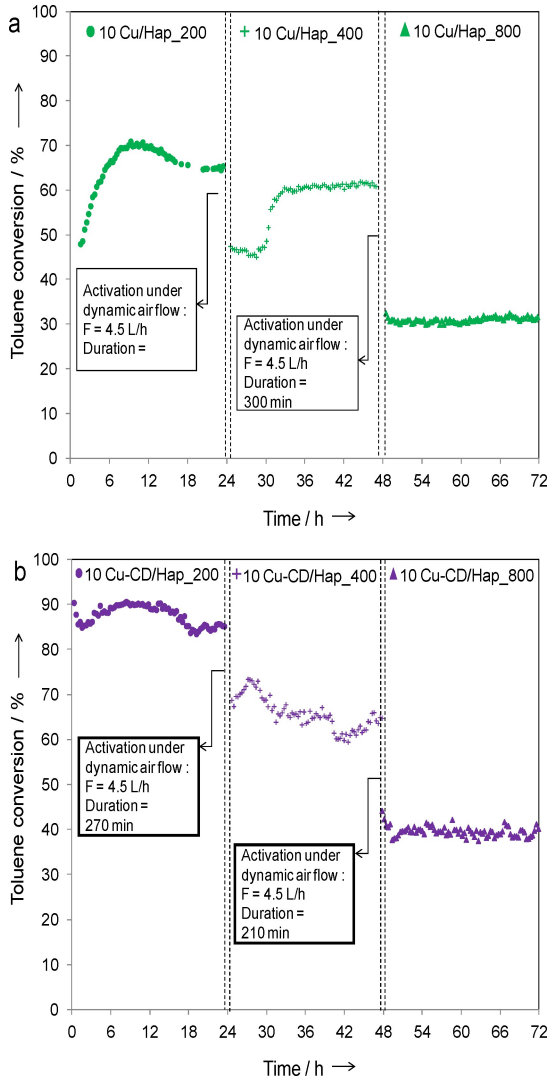

Figure 12. Time-on-stream plot of toluene conversion at 250 °C over 10 Cu/Hap and 10 Cu-CD/Hap catalysts for three different toluene concentration values: 200, 400, and 800 ppmv.

(200-400-800 ppmv) in dry air for 10 Cu/Hap and 10 Cu-CD/Hap, respectively. Interestingly, the 10 Cu/Hap catalyst undergoes an activation period seen in an increase in toluene conversion as a function of time in the first two stages of the experiment. The first activation period can be connected with the elimination of remaining poisonous surface nitrate species retained on the hydroxyapatite. Anyway, it is observed that the toluene conversion decreases with increasing toluene concentration. The toluene conversion decreases from 65 % to 62 % to 31 % for Cu/Hap and from 85 % to 65 % to 38 % for Cu-CD/Hap at the end of each stage of the experiment. Notably, it is observed for the first two steps of the experiment an induction period before stabilization of the conversion for the Cu/Hap catalyst. In conclusion, the Cu-CD/Hap catalyst exhibits a higher catalytic activity than that observed with Cu/Hap. This behavior can be explained by the presence of highly dispersed copper oxide crystallites of small size and high

reducibility as previously established by XRD, XPS and TPR measurements, respectively, in line with previous reports.

Role of β-CD throughout the preparation of CuO/Hap

Two copper oxide catalysts supported on mesoporous hydroxyapatite were synthesized through impregnation with aqueous solutions containing copper nitrate with or without β-CD. It was found that the presence of β-CD affected the final properties of the copper oxide catalysts, in terms of metal dispersion, reducibility and catalytic behavior in the total oxidation of toluene. The co-impregnation of copper and β-CD over hydroxyapatite was found to promote the catalytic activity through a combined effect of improved dispersion of CuO particles and improved reducibility of copper. CuO/Hap obtained from the β-cyclodextrin assisted synthesis led to the best catalytic performance. Regarding the role of β-CD in dispersing Cu^{2+} species, the formation of $Cu_2(OH)_3(NO_3)$ with a similar average crystallite size of about 45 nm in the dried state with or without β-CD seems to rule out the complexation between the copper precursor and β-CD. When comparing with the β-CD assisted synthesis of Co_3O_4/ZrO_2,[30] while the TM (Transition Metal) precursor was a nitrate salt with a β-CD/cobalt ratio 0.1 in both cases, the two systems differed both by the nature of the cation and support. It was assumed that the nature of the hydroxyapatite which had the ability to undergo cationic and anionic substitution could favor the formation of $Cu_2(OH)_3(NO_3)$ at the expense of the Cu(II)-CD complexes. However, the native cyclodextrin delayed the formation of some CuO NPs that were observed in the conventional impregnation. This finding was related to the identification of direct interactions between cyclodextrin or its degradation by-products with Cu^{2+} and Ca^{2+} of the Hap at the outermost layers of the solid. The presence of β-CD oxidation by-products in close interaction with Cu^{2+} inhibited particle growth during the first stages of the calcination step implying water departure and boosted the decomposition of the precursor phase of oxide at lower temperature allowing an increase of the nucleation sites. Considering that the oxidation of toluene may involve a redox mechanism implying lattice oxygen consumption to be replenished by air from the air stream, the beneficial effect of β-CD addition consists in a better reducibility and dispersion of the CuO NPs on the surface of Hap.

Conclusion

To conclude, we have extended the scope of β-CD for the synthesis by wet impregnation of a novel hydroxyapatite supported copper oxide at a Cu content of 10 wt% for the total oxidation of toluene. Our findings show that the addition of β-CD (β-CD/Cu of 0.1) has strong impact on the properties of the final catalyst in terms of reducibility and dispersion of the active copper species. These characteristic features have been related to the beneficial effect of β-CD on the thermal degradation pathway of the hydroxyapatite supported $Cu_2(OH)_3(NO_3)$ entities detected after the drying step. The β-CD or its degradation products homogeneously distributed on hydroxyhapatite at the first stages of the calcination step can play the role of spacers preventing the growth of the CuO particles as well avoiding the incorporation of NO_3^- in the hydroxyapatite support.

Experimental Section

Material preparation

Synthesis of 10 Cu/Hap and 10 Cu-CD/Hap

The stoichiometric hydroxyapatite (Hap) support, with a Ca/P molar ratio equal to 1.67, was prepared according to a co-precipitation procedure reported previously in literature,[68] corresponding to Equation (1):

$$10\ Ca(NO_3)_2 + 6\ NH_4H_2PO_4 + 14\ NH_3.H_2O \rightarrow\ Ca_{10}(PO_4)_6(OH)_2 + 20\ NH_4NO_3 + 12\ H_2O \quad (1)$$

Prior to the impregnation step, the Hap support is calcined in dry air at 400 °C for 4 h with a heating rate of 2 °C.min^{-1}.

The copper oxide catalyst with a theoretical copper content of 10 wt%, derived from β-CD-assisted synthesis was prepared by a wet impregnation technique inspired by the work of Bai *et al.*:[31] in a round bottom flask, 1.7559 g (7.19 mmol) of copper (II) nitrate trihydrate (Sigma Aldrich, purity ≥ 99 %) was added to 50 mL of an aqueous solution containing 0.8156 g of native β-CD ($C_{42}H_{70}O_{35}$, M = 1134 g.mol^{-1}, Roquette Frères) so as to have a molar ratio of cyclodextrin to copper equal to 0.1. The solution was kept under constant stirring for 2 hours at room temperature. The Hap support (4 g) was then added to the copper-β-CD suspension and then stirred again for 2 supplementary hours. The resulting mixture was placed in a rotary evaporator (Büchi Rotavapor R-114; 60 °C; 20 rpm; 70 mbar) to remove water. The recovered solid was dried overnight in an oven at 80 °C, resulting in a blue colored powder with a tint of green. Then, it was calcined under air flow at 400 °C for 10 h, leading to a dark gray powder. The so-obtained catalyst is denoted as 10 Cu-CD/Hap. A conventional copper oxide catalyst (Cu loading: 10 wt%), prepared with the same procedure, but without addition of β-CD and with a smaller calcination time at 400 °C (4 h instead of 10 h) is designated as 10 Cu/Hap. This conventional catalyst was characterized by a blue color after drying step and a light grey color after calcination step. Dried samples are labeled with the suffix D.

Characterization

X-ray diffraction (XRD)

Powder XRD measurements were performed on a laboratory X-ray diffractometer (Bruker AXS D8 Advance powder diffractometer equipped with a LynxEye Super Speed detector) using a Cu–Kα radiation (λ = 1.5418 Å), with a step of 0.02° in the 2θ range of 10–55° and a count time of 5 s. The sample was ground gently, then filled in the depression of the XRD sample holder and smoothed flat. Crystalline phases' identification was made using EVA software, by comparison to reference patterns registered in Powder Diffraction Files (PDF) of the International Centre for Diffraction Data (ICDD) database. The Scherrer equation given below, was employed for the calculation of the mean crystallite size of Hap supported Cu catalysts derived from both conventional and β-CD-assisted synthesis [Equation (2)]:

$$D\ (Å) = \frac{k\lambda}{\beta\cos\theta} \quad (2)$$

where D is the crystallite size in Angström, k a dimensionless shape factor taken as 0.9. λ is the wavelength of the Kα radiation in Angström, θ the diffraction angle in radians and β full peak width at half-maximum intensity in radians after subtracting the instrumental line broadening using LaB_6 as an internal reference.

Raman spectroscopy

Raman spectra were recorded using an XploRA PLUS Raman Microscope (HORIBA Jobin Yvon). Raman analysis was conducted using a laser wavelength of 532 nm with an output power of 20 mW, which was reduced by attenuation filters to 0.2 mW on the sample. The presented spectra corresponded to the average of 5 scans with 1800 s acquisition time for each scan. Preceding Raman analysis a calibration step was performed using a silicon wafer characterized by the Si line $\lambda = 520.6\ cm^{-1}$. A color camera linked to the software allowed the sample to be visualised and the image to be captured on the computer and saved.

UV-visible/DR

Diffuse reflectance spectra (DRS) of the samples were recorded at room temperature between 200 and 900 nm with a resolution of $2\ cm^{-1}$ using a Perkin Elmer Lambda 650 optical spectrometer equipped with a diffuse reflectance accessory.

Thermal Analysis coupled with Mass Spectrometry (TGA/DSC-MS)

A TA Balance instrument, model: SDT 2960 DSC-TGA X, was used to conduct thermal analysis (TGA/DSC) under an atmosphere of 20% O_2 in He (100 $mL.min^{-1}$). The sample was heated at a rate 5 °C.min^{-1} from 25 °C to 1000 °C. A Pfeiffer vacuum Omnistar GSD 320 mass spectrometer was coupled to the exit of the TGA analysis instrument, allowing the monitoring of the following selected m/z signals: m/z = 12, 14, 16, 17, 18, 28, 30, and 44.

Temperature Programmed Reduction coupled with Mass Spectrometry (H_2-TPR/MS)

The H_2-temperature-programmed reduction (H_2-TPR) experiments were conducted using a Micromeritics Autochem II (2920) instrument, equipped with a U-shaped quartz reactor. Prior to starting the analysis, fresh (200 mg) and used catalysts (100 mg) were treated in Ar at 150 °C for 1 h. After cooling down, the H_2-TPR measurements were conducted in 5 vol% H_2/Ar gaseous mixture (50 $mL.min^{-1}$) from room temperature to 800 °C (10 °C.min^{-1}). The amount of consumed H_2 was measured by a thermal conductivity detector (TCD) and calculated from the integrated peak areas of the profiles. The produced water was confined in a cold trap composed of isopropanol and liquid nitrogen before reaching the detector. The outlet gases were identified through the study of m/z signals, acquired by coupling the H_2-TPR instrument with a mass spectrometer (MS).

Time-of-flight secondary ion mass spectrometry (ToF-SIMS)

Time of flight secondary ion mass spectroscopy (ToF-SIMS) data were acquired using a ToF-$SIMS_5$ spectrometer (ION-TOF GmbH Germany) equipped with a bismuth liquid metal ion gun (LMIG).

X-ray photoelectron spectroscopy (XPS)

XPS analysis was performed on an AXIS Ultra DLD Kratos spectrometer equipped with a monochromatic Al–Kα source (hν = 1486.6 eV), operating at 120 W. Irradiation is performed at ambient temperature, under ultra-vacuum conditions (base pressure: 10^{-9} mbar). The photoelectron spectra were calibrated using the C 1s signal detected at a binding energy of 284.8 eV from contaminant carbon. Data treatment was conducted using CasaXPS software. Two recordings of Cu 2p core level XPS spectra were carried out: one at the beginning and one at the end of XPS analysis, in order to monitor the potential occurrence of an XPS-induced reduction of copper particles during data acquisition. Finally, XPS quantification was performed from the study of peak core levels of Ca 2p, P 2p, Cu 2p, and O 1s.

Catalytic activity test

Toluene catalytic oxidation experiments were carried out at atmospheric pressure using a continuous-flow fixed-bed reactor located in an electrical furnace. For each catalytic run, 200 mg of powder catalyst ($100 < \varphi < 200$ μm) was placed into the microreactor. The catalysts were activated 2 h at 390 °C in a dry air flow (75 $mL.min^{-1}$) before being submitted to the reactive gas atmosphere (~ 800 ppmv of toluene diluted in synthetic air) at a flow rate of 100 $mL.min^{-1}$ for 1 h (VHSV ≈ 30 L g^{-1} h^{-1}). Catalyst performances were evaluated at 390–25 °C with a decreasing rate of 0.5 °C.min^{-1}. The concentrations of the gaseous reactants and products were analyzed online using a 7860 A Agilent Gas Chromatograph equipped with two detectors (a thermal conductivity detector (TCD) and a flame ionization detector (FID)) connected, respectively, to two columns (Restek Shin Carbon ST/Silco HP NOC 80/100 micro packed and capillary column Cp-Wax52CB 25 m, Ø = 0.25 mm).

Toluene conversion into CO_2 (%) was evaluated by Equation (3):

$$C_{CO2} = \frac{[CO_2] \times 100}{7 \times [\text{toluene}]_i} \quad (3)$$

in which $[CO_2]_t$ was the CO_2 outlet concentration and $[\text{toluene}]_i$ was the toluene inlet concentration.

The stability tests for 72 h were performed at atmospheric pressure and a temperature of 250 °C in a continuous-flow fixed-bed Pyrex reactor. For each test, 200 mg of catalyst were placed in the reactor which was set in an electric furnace. Two thermocouples were employed, one fixed to the exterior of the reactor and one placed into a thermowell, positioned in the middle of the catalyst bed, in order to perform an ongoing monitoring of the reaction temperature. The reactive gas mixture consisted first of 200 ppmv (from 0 to 24 h), then 400 ppmv (from 24 to 48 h) and finally 800 ppmv (from 48 to 72 h) of toluene diluted in dry air (100 $mL.min^{-1}$) corresponding to a gas hourly space velocity (GHSV) of 14,500 h^{-1}. Prior to each stability test, the samples were activated in dry air at 390 °C for 2 h (75 $mL.min^{-1}$). Then, the temperature was decreased to 250 °C, and the catalyst was exposed to the reactive gaseous mixture for 72 h. The catalyst was kept in flowing air (90-300 min) during the stabilization of the new toluene concentration. At the end of each stability test, no more reactive gaseous mixture was sent to the catalyst, the furnace was turned off and the system cooled down to room temperature under static conditions. The concentrations of the gaseous reactants and products were assessed by gas chromatograph (7860 A Agilent Gas Chromatograph) equipped with two detectors and two columns: a Thermal Conductivity Detector (TCD) that identifies permanent gases (CO,

CO_2, etc.), separated on a Restek Shin Carbon ST/Silco HP NOC 80/100 micro packed column; and a Flame Ionization Detector (FID) that recognizes hydrocarbons and aromatic compounds (toluene, benzene, etc.), separated on a capillary column CP-Wax 52 CB: 25 m, Ø 0.25 mm × 1.2 μm.

Toluene conversion (C_t) was evaluated by the following equation:

$$C_t\ (\%) = \frac{[\text{toluene}]_i - [\text{toluene}]_t}{[\text{toluene}]_i} \times 100 \quad (3)$$

where $[\text{toluene}]_i$ and $[\text{toluene}]_t$ correspond to toluene inlet and outlet concentrations, respectively.

Acknowledgements

This research is supported by a European Program INTERREG V France-Wallonie-Flanders (FEDER) (DepollutAir). The Chevreul Institute is thanked for its help in the development of this work through the ARCHI-CM project supported by the "Ministère de l'Enseignement Supérieur de la Recherche et de l'Innovation", the region "Hauts-de-France", the ERDF program of the European Union and the "Métropole Européenne de Lille". The authors thank Nicolas Nuns, Pardis Simon, Laurence Burylo, Martine Trentesaux and A. Moissette for their contribution in ToF-SIMS, XPS, XRD, Raman spectroscopy and UV-visible spectroscopy, respectively.

Conflict of Interest

The authors declare no conflict of interest.

Data Availability Statement

Research data are not shared.

Keywords: catalytic oxidation · copper · cyclodextrins · hydroxyapatite · toluene

[1] J.-F. Lamonier, *Catalysts* **2016**, *6*, 7.
[2] J. Quiroz Torres, S. Royer, J.-P. Bellat, J.-M. Giraudon, J.-F. Lamonier, *ChemSusChem* **2013**, *6*, 578–592.
[3] S. Ojala, S. Pitkäaho, T. Laitinen, N. N. Koivikko, R. Brahmi, J. Gaálová, L. Matejova, A. Kucherov, S. Päivärinta, C. Hirschmann, T. Nevanperä, M. Riihimäki, M. Pirilä, R. L. Keiski, *Top. Catal.* **2011**, *54*, 1224–1256.
[4] Y. Guo, M. Wen, G. Li, T. An, *Appl. Catal. B* **2021**, *281*, 119447.
[5] J. K. Edwards, B. Solsona, P. Landon, A. F. Carly, A. Herzing, C. Kiely, G. J. Hutching, *J. Catal.* **2005**, *236*, 69–79.
[6] M. Hosseini, S. Siffert, H. L. Tidahy, R. Cousin, J.-F. Lamonier, A. Aboukaïs, A. Vantomme, B.-L. Su, *Catal. Today* **2007**, *122*, 391–396.
[7] R. Averlant, S. Royer, J.-M. Giraudon, J.-P. Bellat, I. Bezverkhyy, G. Weber, J.-F. Lamonier, *ChemCatChem* **2014**, *6*, 152–161.
[8] J. Quiroz, J.-M. Giraudon, A. Gervasini, C. Dujardin, C. Lancelot, M. Trentesaux, J.-F. Lamonier, *ACS Catal.* **2015**, *5*, 2260–2269.
[9] M. Zimowska, A. Michalik-Zym, R. Janik, T. Machej, J. Gurgul, R. P. Socha, J. Podobin'ski, E. M. Serwicka, *Catal. Today* **2007**, *119*, 321–326.
[10] D. Romero, D. Chlala, M. Labaki, S. Royer, J.-P. Bellat, I. Bezverkhyy, J.-M. Giraudon, J.-F. Lamonier, *Catalysts* **2015**, *5*, 1479–1497.
[11] C.-H. Wang, *Chemosphere* **2004**, *55*, 11–17.
[12] S. M. Saqer, D. I. Kondarides, X. E. Verykios, *Top. Catal.* **2009**, *52*, 517–527.
[13] S. A. C. Carabineiro, X. Chen, M. Konsolakis, A. C. Psarras, P. B. Tavares, J. J. M. Orfao, M. F. R. Pereira, J. L. Figueiredo, *Catal. Today* **2015**, *244*, 161–171.
[14] M. Ibrahim, M. Labaki, J.-M. Giraudon, J.-F. Lamonier, *J. Hazard. Mater.* **2020**, *383*, 121–139.
[15] A. Fihri, C. Len, R. S. Varma, A. Solhy, *Coord. Chem. Rev.* **2017**, *347*, 48–76.
[16] S. Campisi, M. G. Galloni, F. Bossola, A. Gervasini, *Catal. Commun.* **2019**, *129*, 79–85.
[17] Y. Xin, T. Shirai, *Sci. Rep.* **2021**, *11*(1), 7512.
[18] H. Nishikawa, T. Oka, N. Asai, H. Simomichi, T. Shirai, M. Fuji, *Appl. Surf. Sci.* **2012**, *258*, 5370–5374.
[19] Y. Xin, H. Ikeuchi, J. Hong, H. Nishikawa, T. Shirai, *J. Ceram. Soc. Jpn.* **2019**, *127*, 263–266.
[20] H. Li, Y.-J. Zhu, *Energy Environ. Mater.* **2021**, *4*, 544–561.
[21] B. Li, Z. Wang, Y. Li, Y. Zhang, Y. He, P. Song, R. Wang, *Chem. Lett.* **2022**, *51*, 5–8.
[22] B. Li, Y. Li, J. Ren, F. Dai, Y. Zhang, Y. He, P. Song, R. Wang, *ACS Appl. Nano Mater.* **2021**, 9370–9381.
[23] Z. Qu, Y. Sun, D. Chen, Y. Wang, *J. Mol. Catal. Chem.* **2014**, *393*, 182–190.
[24] D. Chlala, J.-M. Giraudon, N. Nuns, M. Labaki, J.-F. Lamonier, *ChemCatChem* **2017**, *9*, 2275–2283.
[25] D. Prochowicz, A. Kornowicz, J. Lewiński, *Chem. Rev.* **2017**, *117*, 13461–13501.
[26] E. Norkus, *J. Inclusion Phenom. Macrocyclic Chem.* **2009**, *65*, 237–248.
[27] S. Z. Pan, L. X. Song, L. Bai, M. Wang, J. H. Zhu, J. Chen, *Curr. Org. Chem.* **2011**, *15*, 862–868.
[28] L. X. Song, S. Z. Pan, L. Bai, Z. Dang, M. Wang, F. Y. Du, J. Chen, *Supramol. Chem.* **2011**, *23*, 447–454.
[29] N. Morin-Crini, S. Fourmentin, E. Fenyvesi, E. Lichtfouse, G. Torri, M. Fourmentin, G. Crini, *Environ. Chem. Lett.* **2021**, *19*, 2581–2617.
[30] A. Jean-Marie, A. Griboval-Constant, A. Y. Khodakov, E. Monflier, F. Diehl, *Chem. Commun.* **2011**, *47*, 10767–10769.
[31] L. Bai, F. Wyrwalski, J.-F. Lamonier, A. Y. Khodakov, E. Monflier, A. Ponchel, *Appl. Catal. B* **2013**, *138*, 381–390.
[32] L. Bai, F. Wyrwalski, M. Safariamin, R. Bleta, J.-F. Lamonier, C. Przybylski, E. Monflier, A. Ponchel, *J. Catal.* **2016**, *341*, 191–204.
[33] Y. Chen, Y. Liu, D. Mao, J. Yu, Y. Zheng, X. Guo, Z. Mab, J Taiwan, *Inst Chem Eng* **2020**, *113*, 16–26.
[34] H. W. Richardson, « Copper Compounds », in *Kirk-Othmer Encyclopedia of Chemical Technology*, American Cancer Society, **2003**, 767–783.
[35] I. V. Morozov, K. O. Znamenkov, Y. M. Korenev, O. A. Shlyakhtin, *Thermochim. Acta* **2003**, *403*, 173–179.
[36] M. Galera Martínez, D. Pham Minh, E. Weiss-Hortala, A. Nzihou, P. Sharrock, *Compos. Interfaces* **2013**, *20*, 647–660.
[37] M. S. Zarif, A. R. Afidah, J. M. Abdullah, A. R. Shariza, *Biomed. Res.-INDIA* **2012**, *23*, 513–520.
[38] S. Khan, J. Boateng, *Polymer* **2018**, *10*, 157.
[39] X. Xiao, R. Liu, C. Qiu, D. Zhu, F. Liu, *Mater. Sci. Eng. C* **2009**, *29*(3), 785–790.
[40] Z. Stojanovic, L. Veselinovic, S. Markovic, N. Ignjatovic, D. Uskokovic, *Mater. Manuf. Processes* **2009**, *24*(10-11),1096–1103.
[41] V. Hayez, V. Costa, J. Guillaume, H. Terryn, A. Hubin, *Analyst* **2005**, *130*(4), 550–556.
[42] D. C. Pereira, D. L. A. de Faria, V. R. Constantino, *J. Braz. Chem. Soc.* **2006**, *17*, 1651–1657.
[43] J. Chrzanowski, J. C. Irwin, *Solid State Commun.* **1989**, *70*, 11–14.
[44] W. M. Keely, H. W. Maynor, *J. Chem. Eng. Data* **1963**, *8*, 297–300.
[45] I. Schildermans, J. Mullens, B. J. Van der Veken, J. Yperman, D. Franco, L. C. Van Poucke, *Thermochim. Acta* **1993**, *224*, 227–232.
[46] R. A. Friedel, J. L. Shultz, A. G. Sharkey, *Anal. Chem.* **1959**, *31*, 1128–1128.
[47] S. Kohata, K. Jyodoi, A. Ohyoshi, *Thermochim. Acta* **1993**, *217*, 187–198.
[48] X. Xiao, R. Liu, C. Qiu, D. Zhu, F. Liu, *Mater. Sci. Eng. C* **2009**, *29*, 785–790.
[49] F. Trotta, M. Zanetti, G. Camino, *Polym. Degrad. Stab.* **2000**, *69*, 373.
[50] V. Miskovic-Stankovic, S. Erakovic, A. Jankovic, M. Vukašinović-Sekulić, M. Mitrić, Y. C. Jung, S. J. Park, K. Y. Rhee, *Carbon Lett.* **2015**, *16*, 233–240.
[51] F. E. Tabaght, K. Azzaoui, A. Elidrissi, O. Hamed, E. Mejdoubi, S. Jodeh, N. Akartasse, M. Lakrat, A. Lamhamdi, *Int. J. Polym. Mater. Polym. Biomater.* **2020**, 1–12.
[52] J. F. Xu, W. Ji, Z. X. Shen, W. S. Li, S. H. Tang, X. R. Ye, D. Z. Jia, X. Q. Xin, *J. Raman Spectrosc.* **1999**, *30*, 413–415.

[53] W. Wang, Z. Liu, Y. Liu, C. Xu, C. Zhang, G. Wang, *Appl. Phys. A* **2003**, *76*, 417–420.
[54] R. B. Unabia, S. Bonebeau, R. T. Candidato Jr, J. Jouin, O. Noguera, L. Pawłowski, *J. Eur. Ceram. Soc.* **2019**, *39*, 4255–4263.
[55] P. Rulis, L. Ouyang, W. Y. Ching, *Phys. Rev. B Condens. Matter* **2004**, *70*(15), 155104–1-155104-8.
[56] H. Praliaud, Y. Kodratoff, G. Coudurier, M. V. Mathieu, *Spectrochim. Acta Part A* **1974**, *30*, 1389–1398.
[57] J. Guo, H. Yu, F. Dong, B. Zhu, W. Huang, S. Zhang, *RSC Adv.* **2017**, *7*, 45420–45431.
[58] G. Busca, *J. Mol. Catal.* **1987**, *43*(2), 225–236.
[59] H. Praliaud, S. Mikhailenko, Z. Chajar, M. Primet, *Appl. Catal. B.* **1998**, *16*, 359–374.
[60] M. Iwamoto, H. Yahiro, N. Mizuno, W. X. Zhang, Y. Mine, H. Furukawa, S. Kagawa, *J. Phys. Chem.* **1992**, *96*, 9360–9366.
[61] W. Gao, N. Guan, J. Chen, X. Guan, R. Jin, H. Zeng, Z. Liu, F. Zhang, *Appl. Catal. B* **2003**, *46*, 341–351.
[62] E. V. Filimonov, A. I. Shcherbakov, *Prot. Met.* **2004**, *40*, 280–285.
[63] M. C. Biesinger, *Surf. Interface Anal.* **2017**, *49*, 1325–1334.
[64] F. P. J. Kerkhof, J. A. Moulijn, *J. Phys. Chem.* **1979**, *83*, 1612.
[65] W. J. Landis, J. R. Martin, *J. Vac. Sci. Technol. A.* **1984**, *2, 1108–1111*.
[66] L. Silvester, J.-F. Lamonier, R.-N. Vannier, C. Lamonier, M. Capron, A.-S. Mamede, F. Pourpoint, A. Gervasini, F. Dumeignil, *J. Mater. Chem. A* **2014**, *2*, 11073–11524.
[67] S. M. Saqer, D. I. Kondarides, X. E. Verykios, *Top. Catal.* **2009**, *52*(5), 517–527.
[68] M. Ibrahim, M. Labaki, N. Nuns, J.-M. Giraudon, J.-F. Lamonier, *ChemCatChem* **2020**, *383*, 121–139.

Manuscript received: July 27, 2022
Revised manuscript received: October 28, 2022
Accepted manuscript online: November 16, 2022
Version of record online: December 13, 2022